.A New Healing Strategy for Metals: **Programmed Damage and Repair**

SUPPLEMENTARY MATERIAL

Mariia Arseenko, Florent Hannard, Lipeng Ding, Lv Zhao, Eric Maire,

Julie Villanova, Hosni Idrissi, and Aude Simar

1. Manufacturing by Friction stir processing (FSP) and microstructure characterization

Friction Stir Processing (FSP) is a rather newly developed process to modify aluminium alloys and insert particles [1]. A top view of the process is presented in Figure S1. A macrograph of the nugget zone of the new alloy and a microhardness map are provided in Figure S2. The processing parameters are detailed in the Methods section. Figure S2 shows that 16 FSP passes lead to a homogenous distribution of in situ formed particles, as evidenced by scanning electron microscopy (SEM) and optical microscopy as well as by the microhardness map. Samples for microstructural observation and mechanical testing were prepared from the top part of the nugget zone at a depth of at least 0.5 mm, i.e. low enough not to be affected by the proximity of the friction stir tool.

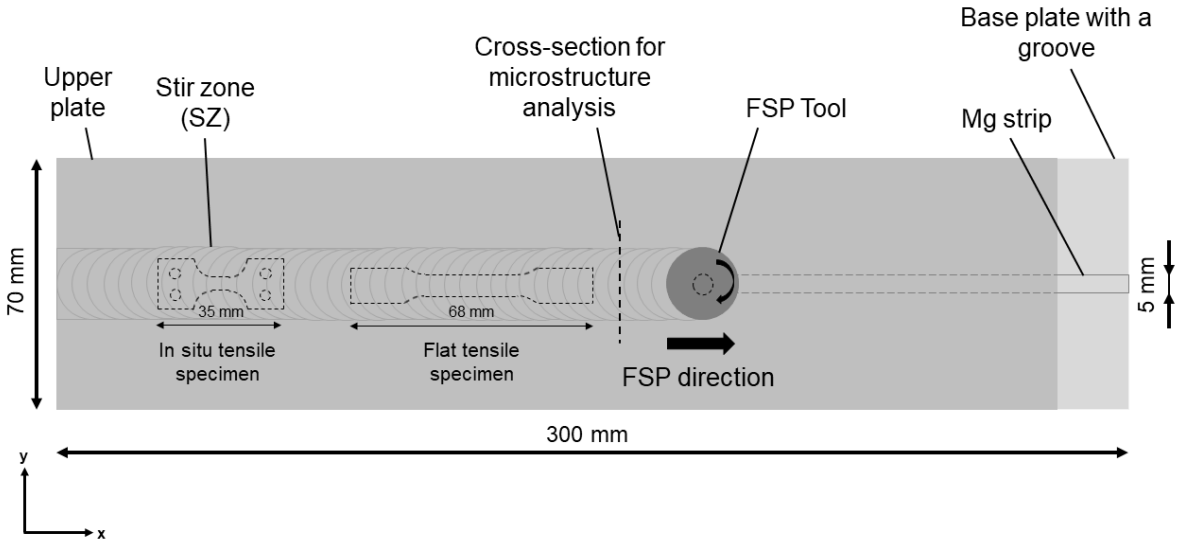

Figure S1. Friction Stir Processing of Al-0.5Mg_2Si alloy (top view)

Table S1 shows modified chemical composition of Al-0.5Mg_2Si alloy compared to Al 6063. An increase in Mg content can be clearly seen. This increase is caused by insertion of pure Mg

strip into the machined groove and its influence to the material microstructure and properties is discussed in the main text, Section 4.

Table S1. Chemical composition of Al 6063-FSP and Al-0.5Mg_2Si alloys

Material	Element, wt.%							
	Al	Mg	Si	Fe	Cr	Mn	Ti	V
Al 6063-FSP	98.6	0.44	0.44	0.24	0.01	0.04	0.02	0.01
Al-0.5Mg_2Si	94.9	3.41	0.40	0.27	0.01	0.04	0.02	0.01

Table S2 shows a comparison of the phases' composition in Al-0.5Mg2Si alloy obtained by EDX analysis and by Thermo-Calc simulation (Thermo-Calc 2019a with TCAL6 – MOBAL5 database) at 490 °C corresponding to FSP operational temperature. The Thermo-Calc simulation at 490 °C with the Al matrix composition corresponds well to the results of TEM analysis (2.8 wt.% versus 3 wt.% measured after FSP and cooling) provided in Figure 4 of the main manuscript. The conclusion is that the fast cooling after FSP was quick enough to keep all the Mg dissolved during FSP (knowing that the solubility of Mg in Al at a room temperature is below 1%). However, the predicted volume fraction of Mg_2Si is significantly larger (1.4 vol.%) than the measured one (0.5 vol.%). This could be the consequence of limitations in the resolution of the characterization techniques. The reason why we believe this, is that no Si is measured in the matrix, suggesting that all Si was consumed for Mg_2Si precipitation.

Table S2. Phases' composition in Al-0.5Mg_2Si alloy

		Experiment	Thermo-Calc at 490 °C
Al matrix:	vol. %	95	98.6
- Al		96.9	97.2
- Mg	wt. %	3	2.8
- Si		0.1	-
Mg_2Si phase:	vol. %	0.5	1.4
- Al		2.3	-
- Mg	wt. %	63.3	63.4
- Si		34.4	36.6

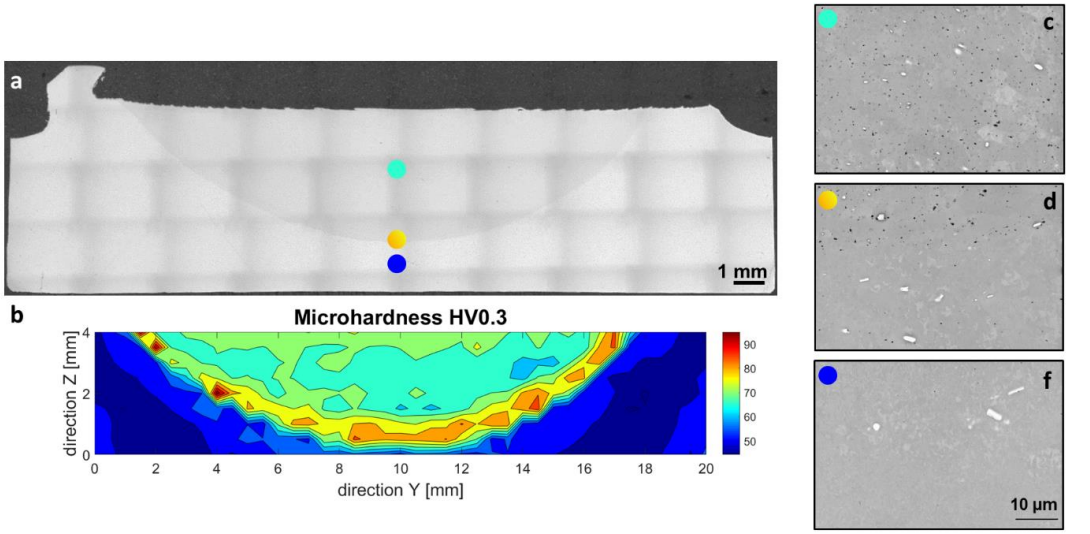

Figure S2. Microstructure of FSPed plate and microhardness map. (a) Optical image of the nugget zone; (b) Microhardness distribution map; (c-f) SEM images corresponding to the color code in (a).

Statistics were performed on SEM images using ImageJ in order to analyze the mean size, distribution and volume fraction of the Mg_2Si particles. For that a threshold was applied in order to extract the particles from the matrix which were then analyzed with "Analyze particles" tool integrated in ImageJ. The results are presented in Figure S3 and Table S3.

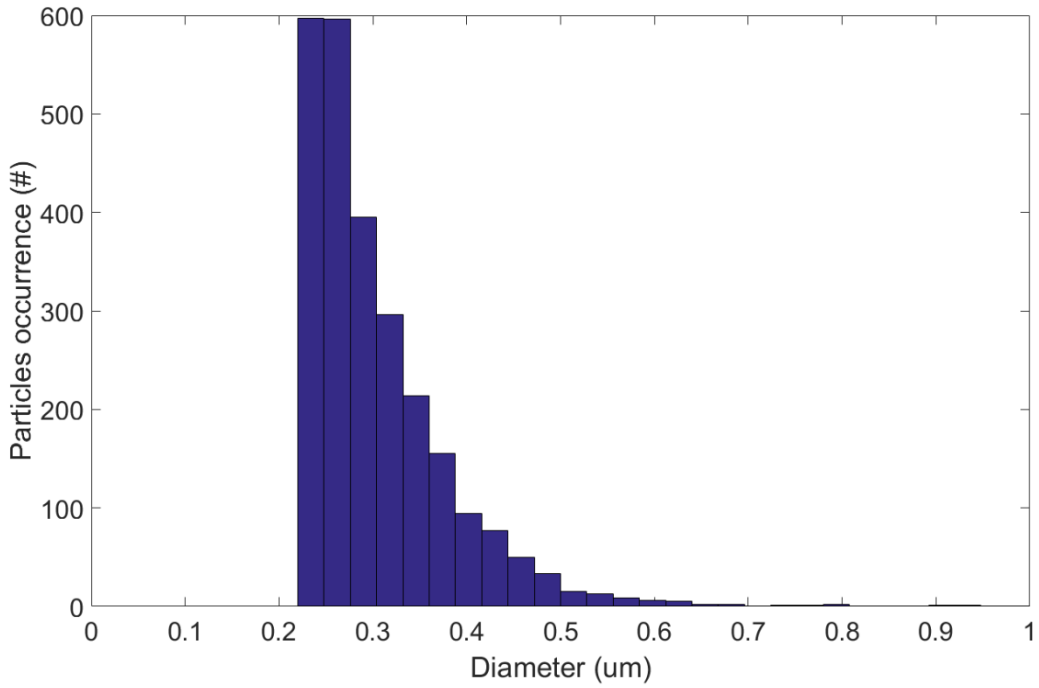

Figure S3. Mg_2Si particles size distribution after FSP

Table S3. Statistics resulting from image analysis of Mg_2Si particles

Total number of particles analyzed	2566
Analyzed area, μm^2	46551
Analyzed particles area, μm^2	199
Particles area fraction, %	0.43
Mean diameter, µm	0.30
Mean near-neighbor distance (NND), µm	1.13

2. Samples for in situ SEM tensile testing, 3D X-Ray nano-imaging and in situ TEM heating experiments

Table S4. List of specimens for 3D X-Ray nano-imaging using holotomography and in-situ TEM

Used for	**Material**	**Specimen n°**	**Pre-strain elongation (Fig. 2b)**	**HHT Temp.**	**Times of heat treatments at which observations were performed [min]**	**Results provided in**
X-Ray nano-imaging heating	Al-0.5Mg_2Si	1	0.6 mm	400 °C	0, 1, 3, 6, 10 min	Figure 6
		2	0.6 mm	400 °C	0, 10, 30, 60, 120, 240 min	Figure 6
		3	0.7 mm	400 °C	0, 10, 30, 60, 120, 240 min	Figure 6
		4	0.6 mm	200 °C	0, 480 min	Figure 5
		5	0.6 mm	300 °C	0, 30, 60, 100 min	Figure 5
	Al6063-FSP	6	0.6 mm	400 °C	0, 60, 120, 240 min	Figure S5a
		7	0.7 mm	400 °C	0, 60, 120, 240, 480 min	Figure S5b
In situ TEM heating	Al-0.5Mg_2Si	8	0.6 mm	400 °C	0, 1, 10, 30 min	Figure 6 + S8-S10

3. Damage evolution during in situ SEM tensile test

In order to demonstrate the damage mechanism modification, in situ tensile test within SEM was performed on the same samples shown in Figure 2a (main manuscript) on two types of samples: Al6063-FSP (Figure S4b, c, d) and Al-0.5Mg_2Si composite (Figure S4e, f, g).

The sample Al6063-FSP (Figure S4b,c,d) exhibits classical void nucleation in Al 6xxx series alloys - on the brittle intermetallics presented in the microstructure at the early stages of loading [2]. Further loading leads to cracks growth on these inclusions (Figure S4d) leading to final fracture.

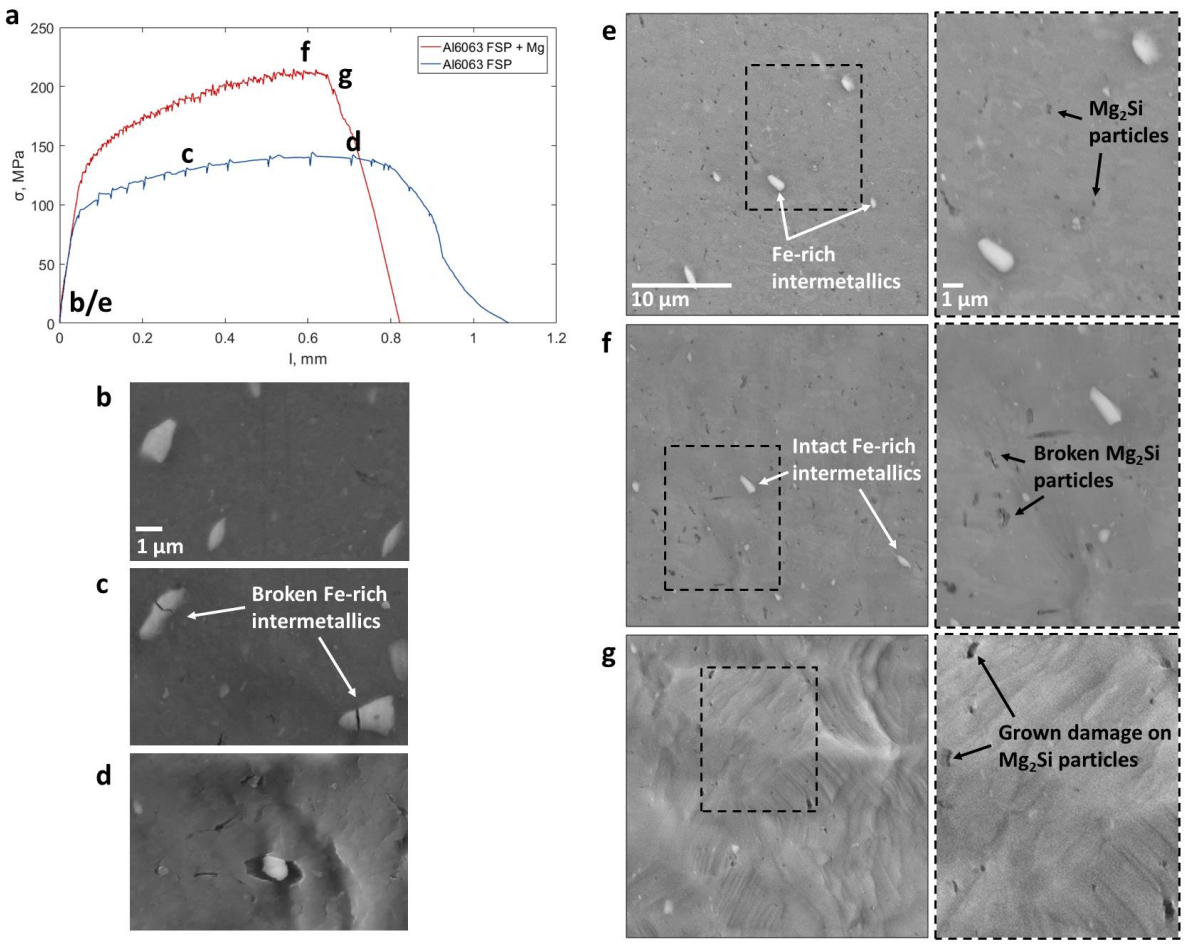

Figure S4. In situ SEM tensile test. (a) Engineering tensile curves for Al-0.5Mg_2Si in red with elongations corresponding to images (e), (f) and (g) and for Al6063-FSP in blue with elongations corresponding to images (b), (c) and (d); (b-d) SEM images obtained during the test for different elongation in Al6063-FSP sample; (e-g) SEM images obtained during the test for different elongation in Al-0.5Mg_2Si sample.

In contrast, the Al-0.5Mg_2Si composite sample exhibits a modified damage mechanism. Damage initiates on small dark grey Mg_2Si sacrificial particles, while Fe-rich intermetallics remain intact. Further loading leads to void growth while additional cracks appear on Mg_2Si particles. In that sample, barely no broken Fe-rich intermetallics were observed before fracture (Figure S4a,g, point g). Moreover, improved yield and ultimate tensile stress can be clearly observed comparing Al6063-FSP and Al-0.5Mg_2Si composite samples. Mg_2Si particles thus have a hardening effect. It is also interesting to note that the first damage observed in Al-0.5Mg_2Si composite sample occurred at a larger global elongation compared to the Al6063-FSP sample. Moreover, as Fe-rich intermetallics did not present damage initiation in Al-0.5Mg_2Si composite, an extended strain range is available for efficiently applying the healing heat treatment.

4. 3D volumes obtained by X-ray holotomography for the comparison sample without Mg addition

In order to confirm that the healing capacity of the FSPed Al-0.5Mg_2Si is unique, an experiment was performed on a specimen produced under the same FSP conditions (hereafter Al 6063-FSP, specimen 6 of Table S3) but without adding the Mg strip (see section 1 of this Supplementary material). The optimum healing temperature (400 °C) was then applied to this specimen. Figure S5 shows that in this case, damage remains unchanged even after 8 hours of HHT. Moreover, a slight growth and shape stabilization (rounding) of void can be observed. Precipitation of a coarse phase in dark grey can also be observed. It is expected that these are Mg_2Si precipitates classically formed and coarsened when long medium-temperature heat treatments are performed on 6XXX series Al alloys [3].

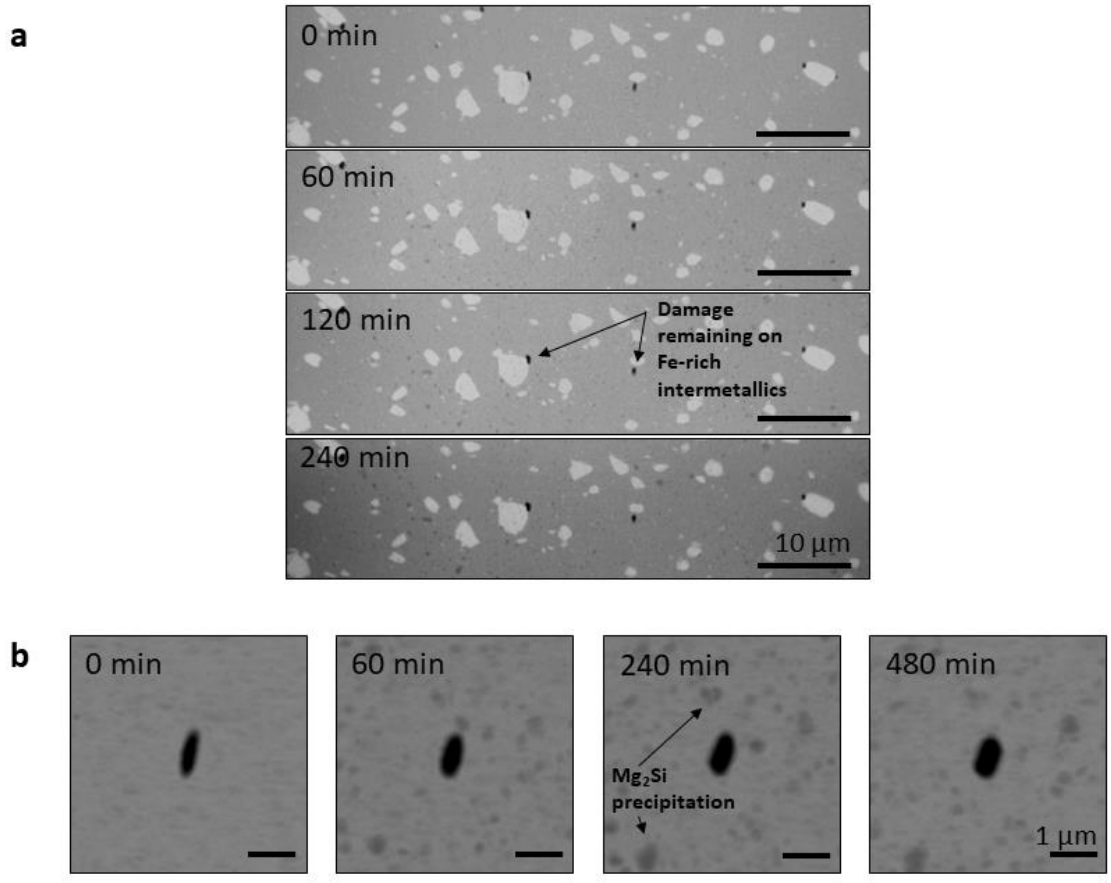

Figure S5. Minimum Intensity Projections (MinIP) of 50 slices of volumes obtained before and after HHT at 400 °C for a Al6063-FSP specimen using X-ray holotomography. (a) Void evolution for a specimen Al6063-FSP; (b) Void tracking (in black) showing its growth and additional precipitation (in dark grey).

5. 3D image analysis and tracking procedure

For each scanning step, cavities were distinguished from the Al matrix by segmentation and their geometrical characteristics were recorded. A tracking algorithm (in-house built toolbox in MATLAB), relying on a graph-based data association approach, has been modified and used to follow the cavities from one scanning step to the next. Only the cavities with initial size above 0.1 µm (i.e. with a diameter of 3 voxels) were used for the tracking procedure in order to avoid counting any noise of the reconstructed images.

An example of graph used for the tracking procedure is shown in Figure S6. Each detection of a cavity in the 3D volume defines a node in the graph, and the cost of an edge between two nodes is defined to decrease with the likelihood that the two nodes correspond to the observations of the same physical cavity at distinct time instants. In this case, the cost of associating two nodes is simply given by the distance between the centroids of the detected cavities. The graph starts and ends with two virtual nodes, called the source and the sink node, respectively. They are connected to all other nodes by creating virtual edges, allowing a sequence of cavities to initiate or terminate at any instant in time. In contrast to regular edges, the cost of a virtual edge is defined as being proportional to the time difference between a node and the source node [$\boldsymbol{\beta_{start} . (t_i - t_{start})}$] or between a node and the sink node [$\boldsymbol{\beta_{end} . (t_{end} - t_i)}$]. Shortest paths are then computed between the source and the sink to find the most probable associations of the cavities along the timeline. More details on the tracking algorithm can be found in Lecarme *et al.* [4], here only the calibration procedure is described (Figure S7). It has been developed in this study in order to select the parameters $\boldsymbol{\beta_{start}}$ and $\boldsymbol{\beta_{end}}$.

The parameters $\boldsymbol{\beta_{start}}$ and $\boldsymbol{\beta_{end}}$, defining the cost of virtual edges, should be calibrated such that the edges between the nodes corresponding to the same cavity in consecutive frames are favored over the virtual edges. On the opposite, when a cavity is disappearing due to healing, the virtual edge linking the node at the last detection of the cavity to the sink should be favored in order to terminate the track. Furthermore, cavities are present in the material from the initial state in this study and thus tracks should start from the initial scan. The calibration procedure is performed as described below:

1) $\boldsymbol{\beta_{start}}$ and $\boldsymbol{\beta_{end}}$ should ensure that most of the voids are tracked from the initial state. This is important in order to ensure that when a track terminates, it corresponds to a cavity disappearing (i.e. healing) and not a missed detection from the tracking algorithm or due to any other source of noise in the measurement. In this study, $\boldsymbol{\beta_{start}}$ and $\boldsymbol{\beta_{end}}$ are selected in order to ensure that at least 95% of the cavities belong to tracks starting from the

initial time. In other words, the fraction of healed cavities should be read as $F_{healed} \pm 0.05^* F_{healed}$.

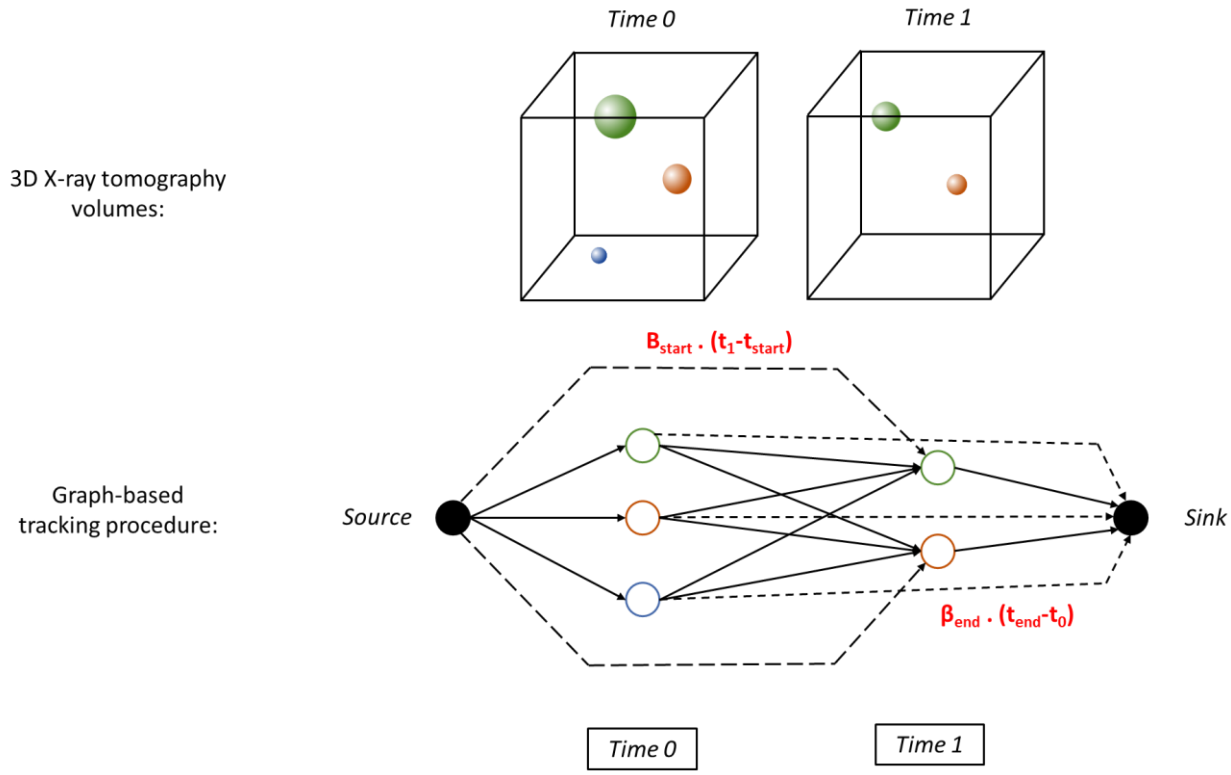

Figure S6. Tracking procedure: Sample graph consisting of two time instants and three detections at initial time and two detections at last time.

2) $\boldsymbol{\beta_{end}}$ should be large enough to link cavities in consecutive frames. However, it should also be small enough to terminate the track when a cavity is disappearing due to healing. Indeed, as can be seen in Figure S6 (top), for $\boldsymbol{\beta_{end}}$ increasing, the maximum displacement of the centroid of all tracked cavities keeps increasing. However, at some point, $\boldsymbol{\beta_{end}}$ becomes too large and there is a jump in the maximum displacement, indicating that "error" tracks start to appear (see Figure S6, bottom), i.e. tracks are connecting different cavities in consecutive frames and $\boldsymbol{\beta_{end}}$ is not well calibrated.
3) $\boldsymbol{\beta_{start}}$ and $\boldsymbol{\beta_{end}}$ are thus modified until points (1) and (2) are satisfied. Since the cavity density might be different from one sample to another, the procedure is performed for each experiment on which the tracking algorithm is applied.

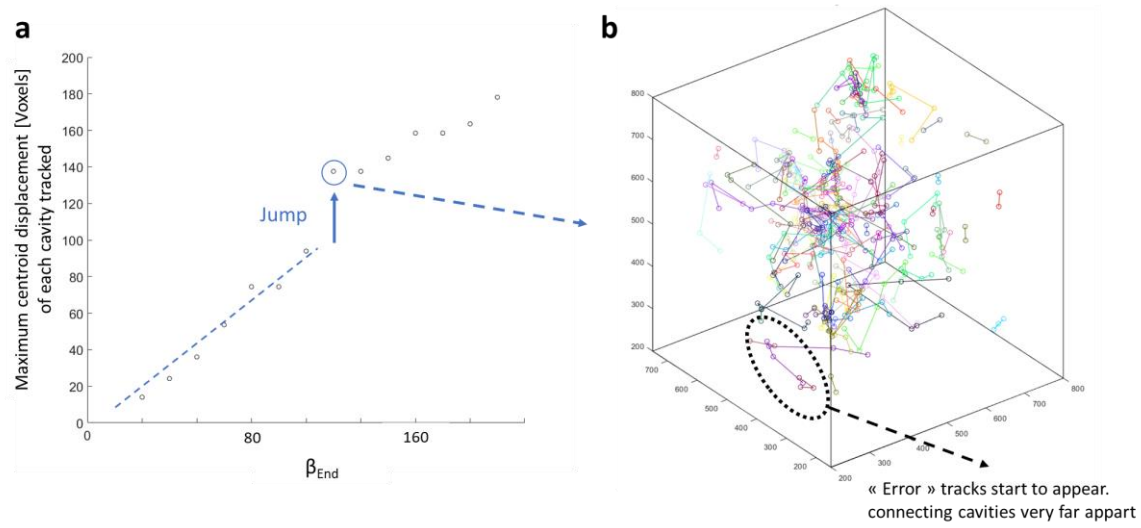

Figure S7. Calibration procedure of the tracking algorithm. (a) Evolution of the maximum centroid displacement (in voxels) found for all tracked cavities, as a function of β_{end}; (b) 3D view of the "error" tracks corresponding to the point indicated in a.

6. In situ heating in the Transmission Electron Microscope

In order to reveal factors influencing healing mechanisms, TEM was used to observe the location of the Mg_2Si particles in the matrix. Figure S8 shows that the reinforcements are mainly located at grain boundaries (see black arrows).

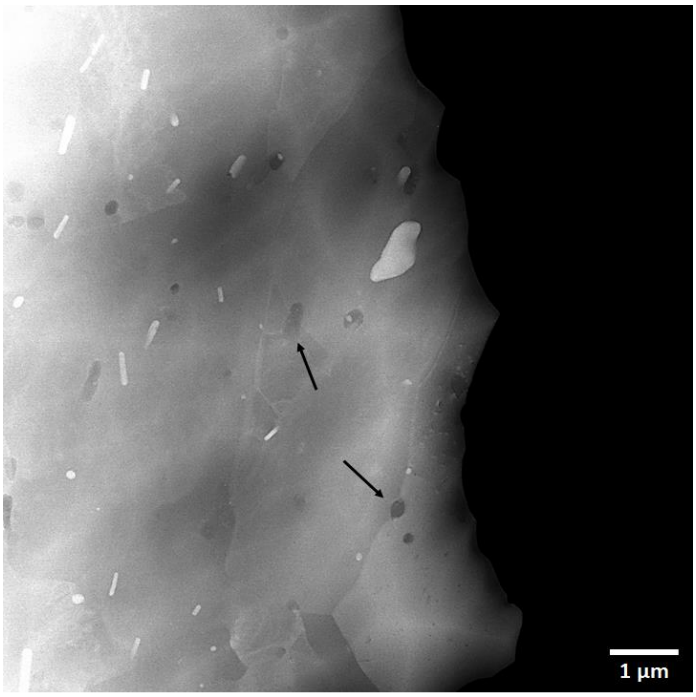

Figure S8. TEM image showing Mg_2Si particles located at grain boundaries. Mg_2Si reinforcements are in dark grey, Fe-rich intermetallics in white.

One of the proposed mechanisms facilitating healing is the high density of defects generated by FSP. In that perspective, Figure S9 shows a grain with dislocations after FSP. Such defects are expected to work as diffusion short-cuts, as mentioned in the main text.

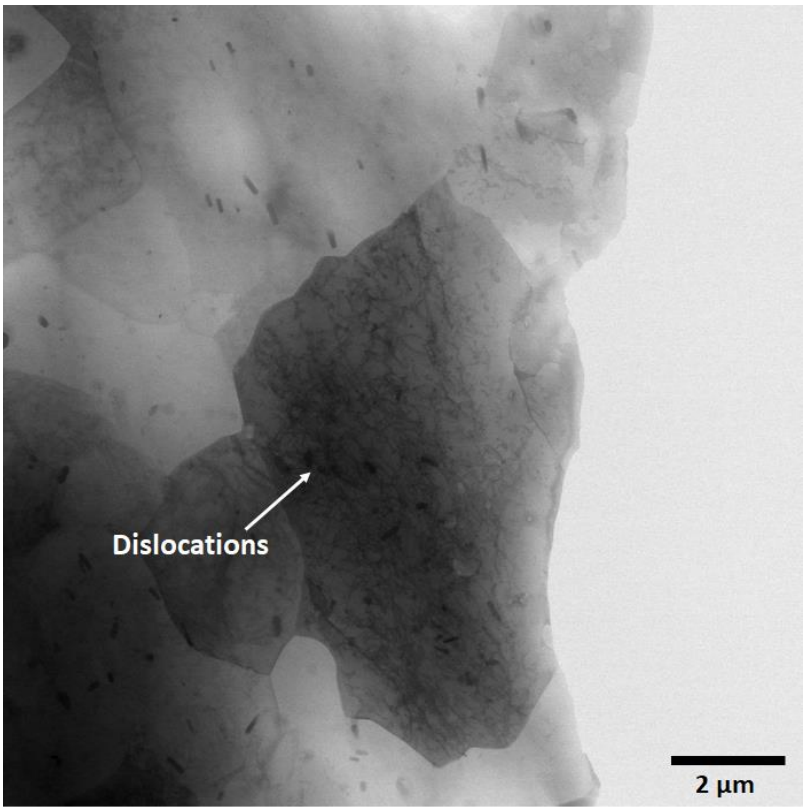

Figure S9. ABF-STEM image showing high density of dislocations as a result of FSP in Al-0.5Mg_2Si sample.

As mentioned in the main text and shown schematically in Figure 1a (main manuscript), damage occurs on the Mg_2Si particles by their fracture or debonding from the matrix. A case of fracture is presented and discussed in the main manuscript (Figure 6e) and the supporting EDX analysis in between heating steps is presented in Figure S10. A layer of the matrix material filling the crack can be clearly seen in Figure S10d.

A case of debonding followed by healing is presented in Figure S11. In this case, a small round particle was debonded from the matrix. This round shape favors particle debonding from the matrix rather than particle fracture. Such damage is in the lower range of the damage size class. It has been shown in Figure 6b (main manuscript) that the kinetics of healing is influenced by a size effect, i.e., smaller damage is healed faster. In addition, a void due to particle debonding from the matrix is surrounded by the matrix, which may also affect the healing kinetics. Indeed, all observed voids due to particle debonding from the matrix are healed only after 1 to 3 min of HHT inside the TEM. However, note that it is difficult to evaluate what is the influence of surface effects (e.g. oxidation and surface diffusion) inherent to TEM specimen size. It thus cannot be legitimately confirmed that these heating durations are comparable to those for bulk specimens, in particular the specimens used for 3D X-ray nano-imaging.

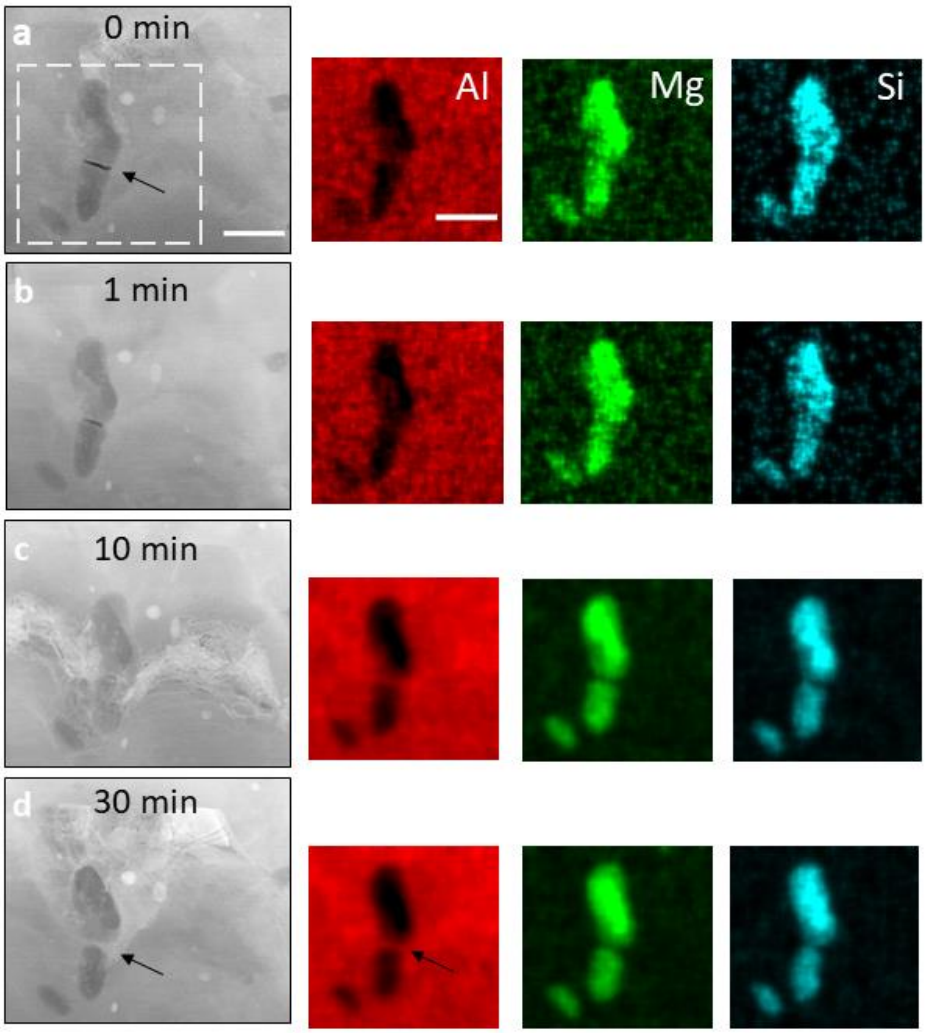

Figure S10. In situ TEM heating experiment at 400 °C. HAADF-STEM images showing the healing evolution with time with corresponding EDX maps for Al, Mg and Si. The area of EDX mapping is delimited by dashed square in a. The scale bars represent 500 nm. The black arrows indicate the position of the crack.

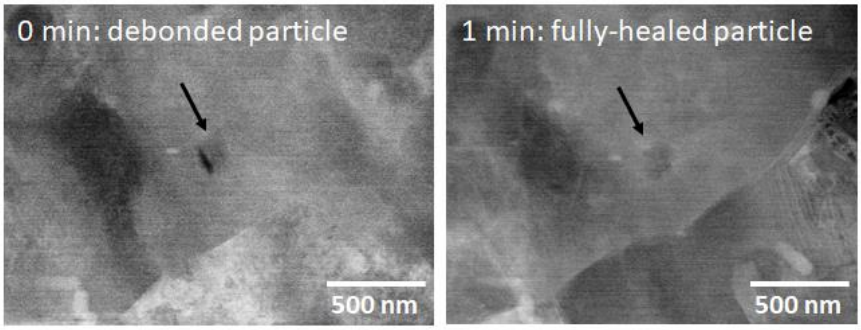

Figure S11. Healing after only 1 min of HHT at 400 °C of a round reinforcement that has debonded from the matrix during prior in situ SEM tensile testing

7. Uniaxial tensile tests

In contrast to previously discussed in situ SEM tensile tests (see Figure 2 of the main text), uniaxial tensile tests to understand the influence of HHT to work of fracture were performed on flat samples cut from the Al-0.5Mg_2Si composite plates. While the samples for in situ SEM tensile test were designed to localize damage in a known region of the sample, the samples for the present tensile tests were designed with the purpose to stop the tensile test prior to necking, in order to ensure uniform deformation in the sample before applying the healing cycle.

Their geometry are presented in Figure S12. Tensile properties were extracted from calculated true stress-strain curves. The true fracture stress (defined as $\sigma_f = F_f/A_f$) and the true fracture strain (defined as $\varepsilon_f = \ln(A_0/A_f)$) were computed from the last force value F_f recorded before fracture, and from the initial and fractured section area, A_0 and A_f , respectively. The fracture area A_f was estimated from the smallest width and smallest thickness at fracture, measured from the reconstituted fractured parts by optical microscopy and subsequent image analysis with ImageJ software. The tensile properties between the necking point and the fracture point are linearly interpolated. In order to identify the work of fracture (W_f) the area under true stress-strain curves was calculated. To evaluate healing ability at least three samples were tested for each condition: (1) as-FSPed (called Al-0.5Mg_2Si); (2) non-damaged but heat treated (called Al-0.5Mg_2Si-HT); (3) damaged, heat treated then loaded until final failure (called Al-0.5Mg_2Si-HHT). The samples Al-0.5Mg_2Si-HHT were strained to 10, 15, 18 and 20% of global elongation before the healing heat treatment (HHT).

The results are presented in Table S5 and the influence of healing treatment on the tensile properties is discussed in the main manuscript.

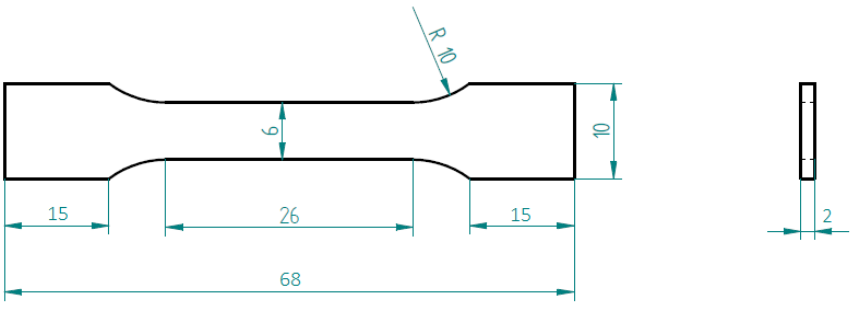

Figure S12. Geometry of flat uniaxial tensile samples

Table S5. Tensile properties of the composite samples before and after the healing heat treatments. The reader is referred to Figure 7 of the main manuscript for representative graphical results. These samples are three Al-0.5Mg_2Si composites: (1) as-FSPed (called Al-0.5Mg_2Si); (2) non-damaged but heat treated (called Al-0.5Mg2Si-HT); (3) damaged, heat treated then loaded until final failure (called Al-0.5Mg_2Si-HHT).

	$E^{a)}$	σ_y [b)]	σ_y[c)]	$\sigma_{Necking}$[d)]	$\sigma_{Failure}$[e)]	ε_f	W_f[c)]	W_f
	[GPa]	[MPa]	[MPa]	[MPa]	[MPa]		[MJ/m^3]	[MJ/m^3]
Al-0.5Mg_2Si (1)	70.9	127.4		279.2	380.9	0.58		175.0
Al-0.5Mg_2Si (2)	68.4	126.5		281.1	407.1	0.65		203.9
Al-0.5Mg_2Si (3)	68.5	120.5		257.3	396.2	0.71		210.1
Al-0.5Mg_2Si (mean)	69.3	124.8		272.53	394.73	0.65		196.3
	±1.2	±3.1		±10.8	±10.7	±0.1		±15.3
Al-0.5Mg_2Si-HT (1)	68.2	132.1		267.8	457.6	0.81		269.1
Al-0.5Mg_2Si-HT (2)	67.0	134.8		246.4	405.2	0.76		226.1
Al-0.5Mg_2Si-HT (3)	66.2	127.6		243.8	387.9	0.72		214.6
Al-0.5Mg_2Si-HT (mean)	67.1	131.5		252.67	416.90	0.76		236.6
	±0.8	±3.0		±10.8	±29.6	±0.00		±23.5
Al-0.5Mg_2Si-HTT (10%)	73.5	123.9	191.0	276.3[b)]	460.1	0.70	245.9	263.9
Al-0.5Mg_2Si-HTT (15%)	65.3	131.1	168.9	252.6[b)]	376.5	0.73	222.3	252.3
Al-0.5Mg_2Si-HTT (18%)	64.0	119.8	167.7	253.3[b)]	425.7	0.77	247.2	282.9
Al-0.5Mg_2Si-HTT (20%)	65.0	127.8	174.8	258.5[b)]	453.1	0.75	254.4	295.8
Al-0.5Mg_2Si-HTT (mean)	67.0	125.7	175.6	260.2[b)]	428.9	0.74	242.5	273.7
	±3.8	±4.2	±9.3	±9.6	±32.8	±0.00	±12.1	±16.8

a) E – Young modulus; b) σ_y - Yield strength; c) data for Post Healing Loading curve; d) $\sigma_{Necking}$ – Strength at necking; e) $\sigma_{Failure}$ – Strength at failure

References

[1] R. Bauri, D. Yadav, Processing Metal Matrix Composite (MMC) by FSP, Butterworth-Heinemann, 2018. doi:10.1016/b978-0-12-813729-1.00003-6.

[2] F. Hannard, A. Simar, E. Maire, T. Pardoen, Quantitative assessment of the impact of

second phase particle arrangement on damage and fracture anisotropy, Acta Mater. 148 (2018) 456–466. doi:10.1016/j.actamat.2018.02.003.

[3] M. Usta, M.E. Glicksman, R.N. Wright, The Effect of Heat Treatment on Mg2Si Coarsening in Aluminum 6105 Alloy, Metall. Mater. Trans. A. 35 (2004) 435–438. doi:10.1007/s11661-004-0354-7.

[4] L. Lecarme, E. Maire, A. Kumar, C. De Vleeschouwer, L. Jacques, A. Simar, T. Pardoen, Heterogenous void growth revealed by in situ 3-D X-ray microtomography using automatic cavity tracking, Acta Mater. 63 (2014) 130–139. doi:10.1016/j.actamat.2013.10.014.